ORCA – Online Research @ Cardiff

Softening and hardening on a Zr-based bulk metallic glass induced by nanosecond laser surface melting

Yang Jiao[1], Emmanuel Brousseau[1]*, Koji Kosai[2], Alexander J G Lunt[3], Jiwang Yan[2], Quanquan Han[1], Hanxing Zhu[1], Samuel Bigot[1], Weifeng He[4]

1. Cardiff School of Engineering, Cardiff University, Cardiff, CF24 3AA, United Kingdom
2. Department of Mechanical Engineering, Faculty of Science and Technology, Keio University, Yokohama, 223-8522, Japan
3. Department of Mechanical Engineering, University of Bath, Bath, BA2 7AY, United Kingdom
4. Institute of Aeronautics Engine, School of Mechanical Engineering, Xi'an Jiaotong University, Xi'an, Shaanxi, 710049, China

Abstract

The study reported here confirms that laser surface melting (LSM) can be employed to modify the hardness and the shear banding behaviour of bulk metallic glasses (BMGs). More specifically, by conducting LSM operations on the Zr-based Vitreloy 105 BMG in ambient atmosphere using a nanosecond laser, it was found that surface hardening can be achieved, in addition to the well-known surface softening effect. Besides, it was found that the presence of compressive residual stress and an increased introduction of crystalline precipitates accompanied LSM-induced surface hardening. On the contrary, tensile residual stress and a reduced fraction of crystalline precipitates were observed for a softened surface post-LSM. Finally, differences in shear-banding mechanisms were detected near the surface of the laser irradiated regions. More specifically, overall reduced serrated flow but important surface shear bands events were observed following the LSM-based introduction of compressive residual stress. In contrast, more pronounced serrated flows and the likely distribution of shear banding activity well beneath the irradiated BMG surface was promoted when LSM resulted in the introduction of tensile residual stress.

Keywords: Laser surface melting, bulk metallic glass, Vitreloy 105，hardness, shear banding behaviour

1. Introduction

It is well-documented that, in comparison with their crystalline counterparts, amorphous alloys, or bulk metallic glasses (BMGs), exhibit high strength and hardness [1], large elastic limit [2] and good corrosion resistance [3]. However, it is also well-known that BMGs generally deform via highly localised individual shear banding events [4, 5]. The initiation and propagation of such shear bands result in very limited macroscopic plasticity before catastrophic failure, thus seriously impeding the applications of BMGs in load-bearing engineering scenarios [6-8]. In recent years, several surface treatment methods have been proposed to improve the plasticity of BMGs without compromising their strength. These include shot peening [9], surface mechanical attrition [10], laser shock peening [11] and laser surface melting [12]. Among these, laser surface melting (LSM) has been demonstrated to be an effective method to improve the plasticity of BMGs as reported in a number of studies in the past decade [12-18]. One of the earliest reports on this topic is from Chen et al. [16], who showed that the compressive plastic strain of a Zr-based BMG could be increased from 0.3% to 5.3% after LSM, while the amorphous nature of the alloy could be retained. Subsequent investigations further confirmed the positive effect of LSM on retarding brittle fracture in BMG substrates. For example, when trialling the LSM process on a Cu-Zr-based BMG, Wu et al. [12] reported that improvements in compressive plastic strain could also be achieved when crystalline precipitates were introduced in the glassy matrix as a result of laser processing. In another example, and while working with a very similar Cu-Zr-based BMG to that of Wu et al. [12], Cheng et al. [18] observed that LSM could also enhance tensile plasticity. Collectively, these studies have suggested that the improved plasticity could be a combination of factors, which include 1) the increase in free volume resulting from the high cooling rate typically associated with localised high-power laser irradiation [16], 2) the influence of residual stress redistribution [16] and 3) the introduction of structural heterogeneities in the glassy matrix [17], such as residual shear bands and/or crystalline phases.

Regardless of the specific physical mechanism, or combination of mechanisms, driving the observed enhanced plasticity of BMGs following laser processing, it is interesting to point out that, in many of the experimental conditions reported to date, LSM was also accompanied by a softening of the irradiated surfaces [14, 16, 17]. Only in a few reports, namely those from Tariq et al. [19], Mudry et al. [20], and more recently, Huang et al. [21], an increase in hardness was observed following laser surface treatment. However, it is also worth noticing that these particular studies were most likely carried

out when ablation, rather than melting, was the dominant processing regime. This was certainly the case for Huang et al. [21] based on the observation of the Scanning Electron Microscope (SEM) images that the authors reported. Tariq et al. [19] and Mudry et al. [20] did not provide such SEM images or made any comments on the topography of the resulting surfaces. However, it is reasonable to suggest that laser ablation was also likely the dominant regime given that the estimated fluence employed (in J/cm^2) was one order of magnitude higher for Mudry et al. [20] and two orders of magnitude higher for Tariq et al. [19], compared to that of Huang et al. [21]. Thus, for practical applications, it is of interest to find out whether the surface hardening of BMGs could also be achieved in the LSM regime, in addition to the well-known LSM-induced surface softening effect.

It is also important to note that in all three studies highlighted above (i.e. Tariq et al. [19], Mudry et al. [20], and Huang et al. [21]), a common observation is that the increase in hardness was always accompanied by the formation of crystalline precipitates. Tariq et al. [19] selected three different laser processing conditions when irradiating an amorphous $Zr_{55}Cu_{30}Al_{10}Ni_5$ workpiece. While the resulting hardness was systematically higher than that of the as-cast specimen, these authors also observed that, as the laser power was raised, and consequently the size of the primary secondary phase increased, the hardness reduced. On the contrary, Mudry et al. [20] found that the hardness of laser irradiated Fe-based amorphous ribbons increased linearly with the percentage increase of the introduced crystalline phase. So far, the report from Huang et al. [21] is the only example in which both hardening and softening effects were observed depending on the laser processing conditions utilised. In this specific study, the well-known Vitreloy 1 amorphous alloy was irradiated in a nitrogen-rich environment. From the range of process parameters selected, these authors found that only one combination led to a hardness value higher than that of the as-cast specimen. Perhaps not surprisingly given the earlier results from Tariq et al. [19] and Mudry et al. [20], the sample with an increased hardness was also the specimen which exhibited the most pronounced laser-induced introduction of a secondary phase.

Given the body of literature reported above, one of the motivations behind the presented study is to investigate whether it is possible to induce surface hardening while still operating in a melting-dominated regime during laser processing. Indeed, if a BMG part is cast near net-shape, it may not be desirable to apply a post-processing

step leading to substantial laser-based material removal on the surface. To achieve this aim, it is proposed to conduct LSM in ambient atmosphere rather than under inert gas shielding, as it has typically been the case in previous research. It is expected that processing in an oxygen environment promotes the formation of nucleation sites, and the subsequent growth of crystalline precipitates. In addition to evaluating the hardness, a further motivation is to assess the residual stress on the surface of irradiated regions. This aspect was not considered in any of three laser-based studies described earlier that led to surface hardening. To achieve this, it is proposed to implement a relatively recent technique, which is still rather unknown in the field of BMG research. This technique relies on micro-scale focused ion beam milling and digital image correlation analysis (see e.g. the review from Lunt and Korsunsky [22]). With the exception of reports by Cao et al. [23] and Wang et al. [24] in the context of laser shock peening, and by Korsunsky et al. [25] when synthesising a Zr-based BMG, this approach has rarely been employed for residual stress measurements in amorphous alloy research. It is expected that this technique is particularly suited for the current investigation of LSM-induced hardness modification because the literature suggests limited correlation between hardness and compressive residual stress in BMGs (see, e.g. Wang et al. [26]). Thus, traditional hardness tests alone may not be suitable to present a comprehensive assessment of how processing conditions affect the residual stress following LSM treatment. In addition, due to the size limitation of the BMG samples available in this study, compressive or tensile tests could not be conducted to complement the hardness and residual stress measurements by the additional assessment of the plasticity modification induced by LSM. To overcome this issue, nanoindentation tests were carried out as a means to analyse serrated flow characteristics of as-cast and laser irradiated samples, and thus to gain some insights into the localised shear banding behaviour associated with plasticity change under different LSM conditions.

2. Materials and methods

2.1. BMG composition and specimen preparation

The BMG employed in this research is commonly named Vitreloy 105. It is a Zr-based metallic glass that was first synthesised over 20 years ago by Lin et al. [27]. Thus, it is reasonably well-known in the field of BMG studies and nowadays, it can even be purchased commercially from Visser Precision (Denver, USA) as was the case in the present investigation. Alloy ingots with nominal composition $Zr_{52.8}Cu_{17.6}Ni_{14.8}Al_{9.9}Ti_{4.9}$

(at.%) were cast by this company using vacuum injection moulding to produce cylindrical rods 3 mm in diameter and 10 mm in length. Once delivered, these rods were then cut into pieces 3 mm in length using low power micro wire electro-discharge machining (EDM). To help with their subsequent processing and analysis, all samples were embedded in conductive resin, leaving their top surface exposed. To obtain a smooth surface and remove the oxide layer as well as minimise the depth of residual stress that could have formed during EDM, this surface was then mechanically polished to a mirror-like appearance using a succession of 1200 and 2000 grid SiC papers and a 1 µm diamond gel suspension. After polishing, and also after subsequent LSM operations, all specimens were systematically cleaned with acetone in an ultrasonic bath for 15 minutes to remove impurities and small particles from their surface, and then dried in air overnight.

2.2. Laser surface melting

Laser surface melting was carried out using a fibre laser (SPI Lasers, Southampton, United Kingdom), with a wavelength of 1064 nm, a frequency of 80 kHz and a pulse duration of 65 ns. The process parameters that were varied in this study included the beam scanning speed, the laser fluence and the number of irradiation cycles. The spatial profile of the delivered laser beam was near Gaussian with an M^2 value less than 2. The effective diameter of the laser spot was 32 µm. This fibre laser was integrated into a DMG CNC machine tool, which allowed the control of a 3-axis motion platform and the pre-setting of process parameters via the associated machine software. As mentioned earlier, all LSM operations were conducted in ambient atmosphere. The laser was kept stationary to ensure the consistency of the delivered laser energy. Thus, the LSM path on the specimen surface was dictated via the movement of the machine tool stage. The laser beam travelled from a pre-defined starting point of the treated area along a linear direction for a given distance, thus completing one track. The first irradiated spot for the subsequent track was then set at a pre-defined distance increment, i.e. 20 µm. Thus, the overlap between tracks was 37.5%. Unlike laser machining operations, which remove material via melt ejection and vaporisation, LSM aims to melt the irradiated surface without material removal. Therefore, a suitable set of LSM parameters (especially lower laser energy values) were identified in preliminary experiments. The detailed laser parameters used in the present study are shown in Table 1.

Table. 1. Detailed laser parameters used for the LSM experiments.

Wavelength (nm)	Spot diameter (μm)	Pulse duration (ns)	Frequency (kHz)	Track distance (μm)	Laser fluence (J/cm^2)	Scanning speed (mm/s)	Number of irradiation cycles
					3.42	800	1
					3.73	800	1
					3.89	800	1
					4.04	800	1
					4.35	800	1
					4.04	600	1
					4.04	400	1
					4.04	200	1
1064	32	65	80	20	4.04	800	5
					4.04	800	10
					4.04	800	20
					3.42	600	1
					3.42	400	1
					3.42	200	1
					3.42	800	5
					3.42	800	10
					3.42	800	20

2.3. Material characterisation methods

2.3.1. Vickers micro-hardness tests

A Vickers hardness tester (Innovatest, Maastricht, Netherlands), with a load of 2 kg and a dwell time of 10 s, was accessed to measure the Vickers micro-hardness distribution on the surface of the Vitreloy 105 specimens before and after the LSM operations. The micro-hardness (H_v) was determined with the following expression:

$$H_v = 0.1891\,F/D^2 \tag{1}$$

where F is the load (N) and D is the mean value from the lengths of the two diagonals left by the indent (mm). The hardness on ten randomly selected positions on each surface was measured to obtain a value for each sample. In order to compare the hardness data between different processing conditions, the t-test statistical procedure was applied where a P-value less than 0.05 was considered statistically significant.

2.3.2. Surface topography and microstructure characterisation

An atomic force microscope (XE-100 from Park Systems, South Korea) and a scanning electron microscope (1540 XB from Carl Zeiss, Germany) were used to characterise the topography around hardness indents and cross-sectional profiles of different Vitreloy 105 specimens. For such cross-sectional observations, the specimens were etched for 10 s using a solution of 10 vol.% HF + 90 vol.% H_2O [28], then examined

with the SEM equipment. An X-ray diffraction (XRD) instrument with Cu-Kα (λ =1.789 Å) radiation at 35 kV and 40 mA was also employed in a continuous scan mode to assess the effect of LSM on microstructural changes. The XRD data were collected over a 2θ range of 5~90°, with a step width of 0.02° and a counting time of 0.5 s/step.

2.3.3. FIB/SEM residual stress measurements

Due to the amorphous structure of BMGs, residual stress quantification is challenging using diffraction-based methods. Macro-scale destructive techniques such as hole drilling are also not applicable as these methods do not have the resolution required to capture the highly localised stresses within the first few microns of a sample surface. For this reason, the method relying on micro-scale FIB milling and Digital Image Correlation (DIC) analysis was implemented [29]. Within this study, the Zeiss 1540 XB FIB-SEM was used to incrementally mill micropillars on the surface of considered samples. The introduction of these traction free surfaces leads to stress relaxation within the core, which is recorded by sequential SEM images of the sample surface. For example, a surface in a state of compression will lead to pillar expansion during the milling process, with the inverse being true of a tensile surface stress. DIC is then used to quantify this strain change, which is compared with the results of finite element simulations in order to provide an estimate of the residual stresses originally present within the core.

The samples were mechanically mounted using SEM grip stubs in order to minimise drift during the FIB and SEM procedure. A trench width of 1 μm was used to determine the average residual stress within a 5 μm diameter pillar. At each data point, a milling current of 500 pA and accelerating voltage of 30 kV were then used to incrementally remove 350 nm of material in the shape of an annulus. Between each milling step, tilt corrected secondary electron SEM images were collected using an imaging voltage of 5 kV and current of 2.6 nA. The brightness and contrast of these images were adjusted to maximise surface contrast of the imaged features. In total, 14 milling increments and images were collected at each measurement location in a total time of approximately 30 minutes. Three nominally identical measurements were made on each sample selected for residual stress analysis. These were spaced at approximately 50 μm intervals in order to ensure that the stress state being recorded at each location was nominally influenced by <1% from the previous measurement [22].

In order to process the data, DIC was performed using a freely available MATLAB code specifically developed for this milling geometry [30]. Low resolution DIC was initially performed to correct for bulk drift of the samples, with a reduction factor of 5. Several thousand markers were then digitally selected across the centre of the core where strain relief is known to be uniform [31]. A correlation window size of 15 × 15 pixels was used for automated 2D tracking of the markers through the entire image set. Automated outlier removal following the routine implemented by Lunt et al. [29] was then applied. As a final step, least squares fitting was then used to obtain estimates of strain relief at each milling increment as well as the full strain relief at infinite depth. The following estimates of Young's modulus E=88.6 GPa and Poisson's ratio of v=0.37 [32] were used to convert these strain relief values into estimates of the average residual stress and associated confidence interval at each data point.

2.3.4. Nanoindentation tests

Nanoindentation tests were conducted with a ENT-1100a nanoindentation instrument (Elionix Inc., Japan) using a Berkovich indenter under load-control mode while recording the load-depth (P-h) curves for each test. An indentation load of 100 mN and loading/unloading rates of 2 mN/s were applied. The holding time at the maximum indentation load was set to be 1 s for all tests. For each sample assessed, three nanoindentations were carried out. The distance between two adjacent indents was set to be 50 μm to avoid interaction effects.

3. Results

3.1. Qualitative analysis of the surface topography

SEM micrographs of surfaces irradiated with different laser fluence values, namely 3.42 J/cm^2, 3.84 J/cm^2 and 4.35 J/cm^2, for a fixed scanning speed and after one irradiation cycle only, are shown in Fig. 1. It can be clearly seen from this figure that, under the lowest laser fluence considered (3.42 J/cm^2), no obvious craters were formed on the surface. However, flake-type features are apparent between laser tracks. It is suggested that these features are remains of the original oxide layer on the surface of the as-cast sample. Indeed, the backscattered electron (BSE) detector image shown in Fig. 1(b) reveals that these features correspond to regions with a darker contrast. Interestingly, on the surface of samples treated with the slightly higher fluence of 3.89 J/cm^2, these flake-type features were not present anymore (see Fig. 1(c)) while the

resulting surface topography is still relatively unchanged. The corresponding BSE detector image shown in Fig. 1(d), shows that the original oxide layer was indeed removed completely in this case. Under the highest laser fluence, (4.35 J/cm^2), overlapped disk-shaped features can be observed. These features, which are 18 μm in diameter and thus, smaller than the laser spot diameter, were formed by re-solidified melt. In addition, a higher magnification image (see Fig. 1(g)) shows that no vapour particles re-deposited on the surface of this sample. This means that even at the highest fluence value selected in this study, laser melting was still the dominant processing regime; as opposed to laser ablation in the reports discussed earlier from Tariq et al. [19], Mudry et al. [20] and Huang et al. [21].
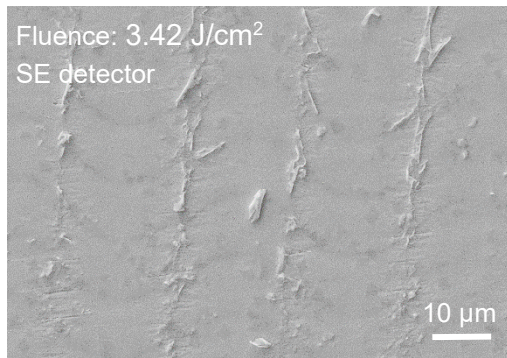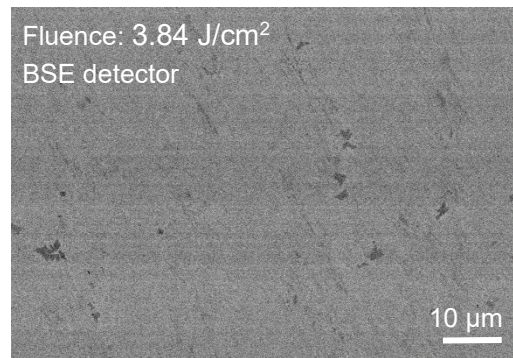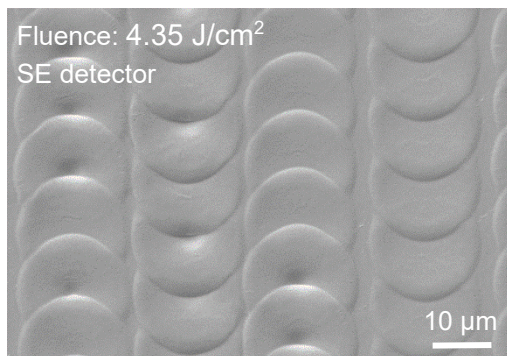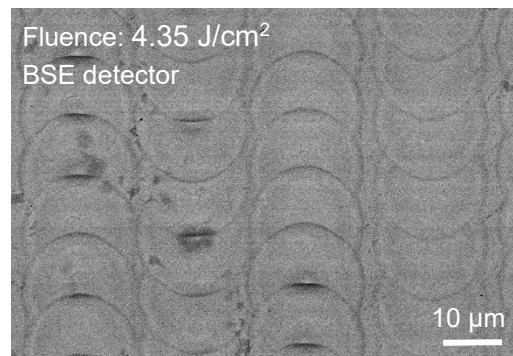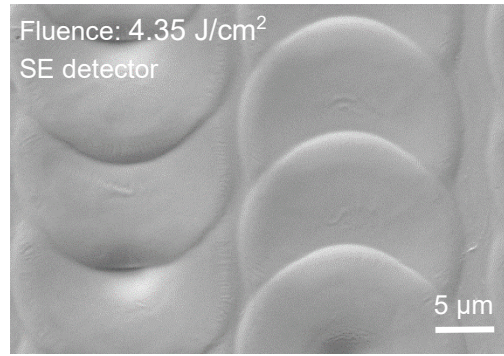

(a)
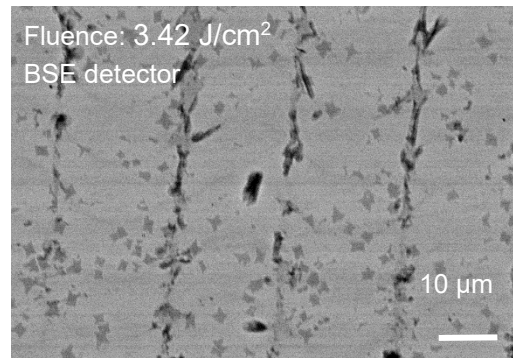
(b)
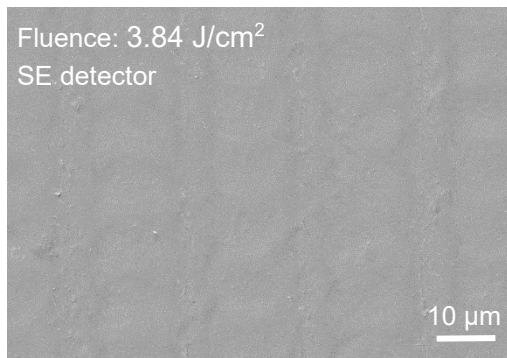
(c)

(d)

(e)

(f)

(g)

Fig. 1 Secondary electron (SE) images of the surface of the Vitreloy 105 BMG following LSM with fluence values of (a) 3.42 J/cm^2 (c) 3.89 J/cm^2 and (e) 4.35 J/cm^2 under a fixed scanning speed of 800 mm/s and one irradiation cycle; (b), (d) and (f) are the corresponding back-scattered electron (BSE) images of (a), (c) and (e), respectively; (g) is a magnified SE image of (e).

3.2. Vickers micro-hardness tests

Hardness is an important property that can affect the wear resistance of metallic glasses. Greer et al. [33] reviewed micro-hardness values of several amorphous alloys available in the literature and their corresponding wear resistance. They reported that, for a given class of alloy composition, the harder the material was, the higher the wear resistance tended to be. Thus, the ability to harden BMGs via LSM could have interesting practical applications where a combination of strength, large elastic limit, corrosion and wear resistance are required, such as in orthopaedic implant materials, for instance. The results of the Vickers micro-hardness tests conducted on the surface of the Vitreloy 105 samples under different LSM processing conditions are presented in Fig. 2. The average hardness of the as-cast sample was measured to be 495.7 HV_2. The standard deviation associated with this data ($\pm$ 7.7 HV_2) was relatively small, suggesting that the hardness distribution on the surface of the as-cast sample was quite homogeneous. In contrast, it is also observed from this figure that, after LSM, micro-hardness values tended to be less homogeneous for all laser processing conditions, as evidenced by larger standard deviations. In particular, for the sample treated with the highest fluence, 4.35 J/cm^2, the standard deviation was also the largest, i.e. $\pm$ 24.7 HV_2, and thus almost threefold that of the as-cast sample. Such a wider spread of hardness values may be attributed to the introduction of laser-induced surface patterns as well as microstructural changes [21].
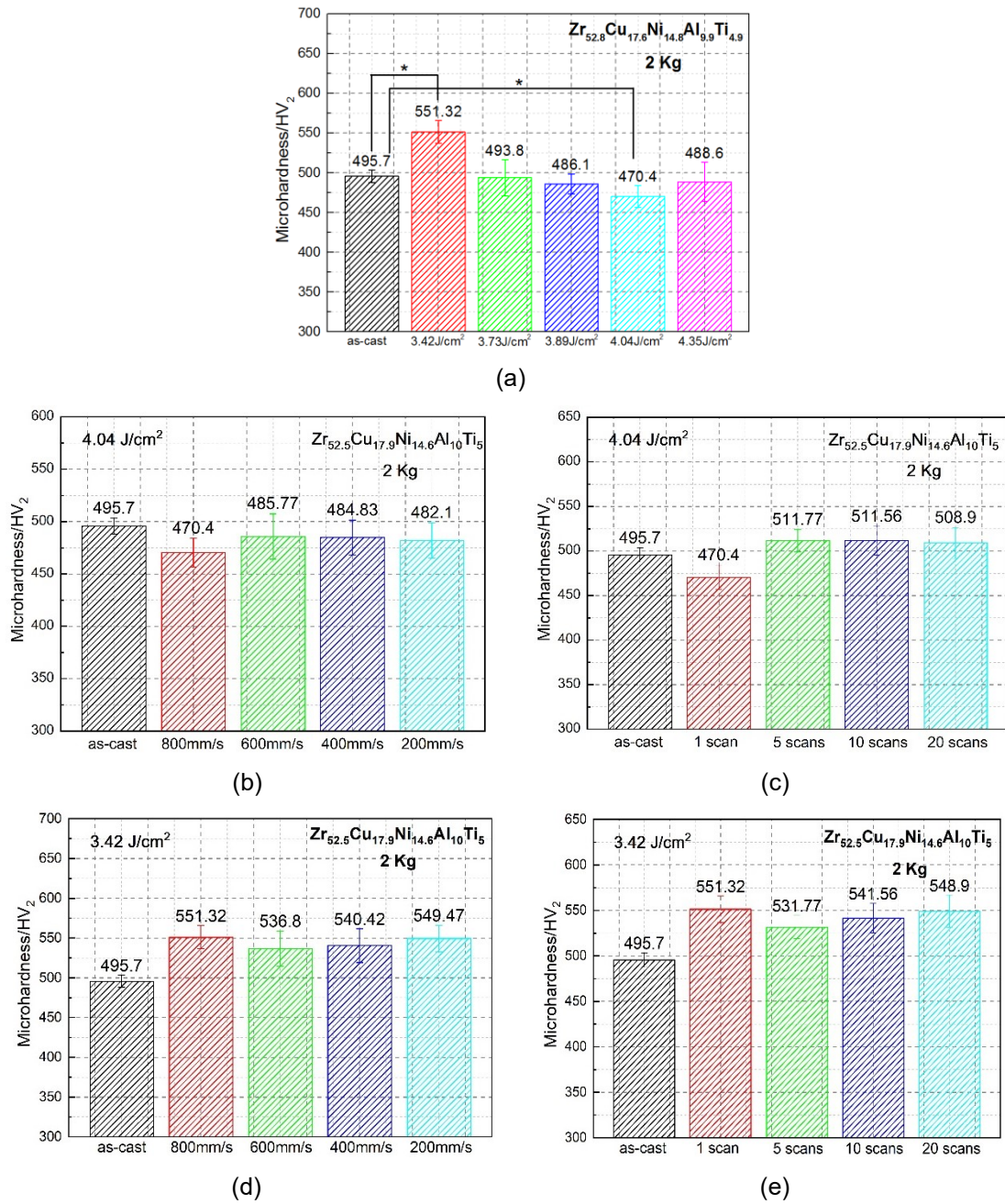
Fig. 2. Surface hardness values of Vitreloy 105 treated with (a) different laser fluence values for a fixed scanning speed of 800 mm/s and one irradiation cycle; (b) different scanning speed values for a fixed fluence of 4.04 J/cm² and one irradiation cycle; (c) various number of irradiation cycles for a fixed fluence of 4.04 J/cm² and a scanning speed of 800 mm/s. The results of the t-test is shown graphically for the data that focussed on the influence of the fluence; in particular, the inclusion of the symbol * in Fig. 2(a) indicates that the means of these sets of data were found to be significantly different from each other.

A comparison of the micro-hardness after LSM for different laser fluence values is provided with the bar chart in Fig. 2(a). Of relevance to one of the motivations of this study, the results indicate that LSM operations could result in surface hardening

depending on the employed laser fluence, in addition to the well-documented softening (see [14, 16, 17, 21] for such reports specifically on Zr-BMG substrates). This effect appears particularly pronounced for the pair of values 3.42 J/cm^2 and 4.04 J/cm^2, which are associated with apparent hardening and softening, respectively. The completion of the t-test confirmed that the mean hardness of 551.32 HV$_2$ for the sample processed with the lower fluence of 3.42 J/cm^2 was statistically different, and thus higher (by 11.2%), than that of the as-cast sample. This test was also employed to confirm that the mean hardness of 470.4 HV$_2$ for the sample processed with the fluence of 4.04 J/cm^2 was lower (by 5.1%) than that of the as-cast sample. Given the relatively small difference between both fluence values, i.e. less than 1 J/cm^2, it is important to note that the hardness on the surface of Vitreloy 105 appears to be very sensitive to variations in delivered energy.

For a single irradiation cycle, the effect of different scanning speed levels on the surface hardness is shown in Fig. 2(b) and Fig. 2 (d) for the fluence values of 4.04 and 3.42 J/cm^2, respectively. In comparison with the effect of the fluence discussed above, it can be observed that the average micro-hardness did not generally vary significantly between scanning speed values. One point to note however, is that the softening effect seen with the fluence of 4.04 J/cm^2 tend to reduce back towards the original hardness with a reduction of the scanning speed. In addition, the effect of the number of irradiation cycles is shown in Fig. 2(c) for a fixed fluence of 4.04 J/cm^2 and a scanning speed of 800 mm/s. From this graph, it can be noted that the micro-hardness reduced compared to that of the as-cast sample when only one irradiation cycle was applied. However, the hardness then increased with additional irradiation cycles and remained relatively stable after 5 cycles. In addition, the outcome of the t-test showed that the mean micro-hardness values could indeed be considered significantly different between 1 cycle and 5 cycles of irradiation. This suggests that this parameter could also be influential on the micro-hardness resulting from LSM, in addition to the effect of the fluence noted earlier. However, given the fact that the micro-hardness remained almost unchanged after a certain number of cycles, it could also be said that there is an effective interval in which the number of irradiation cycles could have such an influence. In the case of a fixed laser fluence of 3.42 J/cm^2 and scanning speed of 800 mm/s, increasing the number of irradiation cycles (see Fig. 2 (e)) retains the overall hardening outcome. Generally, based on the results given in Fig. 2, it could be said that the laser fluence had an important influence on the resulting hardness of the considered Zr-based BMG. For the fluence leading to a hardening effect, a further

change in the scanning speed and the number of cycles does not appear to affect this outcome significantly. However, for the fluence associated with the surface becoming softer, it would seem that increasing the number of irradiation cycles or decreasing the scanning speed tend to reduce or even cancel this effect.

In addition to the results reported above, the effect of the laser fluence on 1) the residual stress distribution, 2) the microstructural evolution and 3) the shear banding behaviour of Vitreloy 105 is presented in the following sections. These subsequent experimental data were obtained for the samples irradiated with the specific fluence values of 3.42 J/cm^2 and 4.04 J/cm^2, for a fixed scanning speed of 800 mm/s and one irradiation cycle. The rationale behind this selection is that this pair of fluence values resulted in the largest hardness increase and decrease, respectively, compared to the original hardness of the as-cast material. The same experimental data were also measured for the as-cast specimen for comparison purpose.

3.3. Residual stress distribution

Residual stress is proven to have a significant effect on mechanical properties, such as the plasticity [6, 23], of bulk metallic glasses. It is known that residual stress can be induced during melting and solidification, phase transformation and mechanical treatment processes [34]. During pulsed LSM, the irradiated BMG surface experiences rapid heating and cooling cycles during which high thermal gradients can be generated along the in-depth direction. As a result, residual stress can be introduced on the target material. Therefore, the effect of LSM on the residual stress distribution was assessed in this research. This was achieved by applying the ring-core FIB milling and DIC technique introduced earlier. A representative example of a ring-core feature milled in the current study is given in Fig. 3. The quantitative results obtained for the as-cast sample and for specimens processed with the selected fluence values of 3.42 J/cm^2 and 4.04 J/cm^2 are given in Fig. 4. In particular, Fig. 4(a) shows the average near-surface residual stress for all three specimens of interest. From this figure, it can be seen that the near-surface residual stress for the sample treated with the lower fluence of 3.42 J/cm^2 presented a compressive state compared to the as-cast material. On the contrary, the introduction of tensile residual stress was detected for the sample treated with the higher fluence of 4.04 J/cm^2. In addition, the individual residual stress measurements for each sample are also reported with Fig. 4(b), (c) and (d). As mentioned earlier, in all cases, three data points were selected from a sample surface

when applying the ring-core FIB milling and DIC technique. It can be seen from these individual residual stress measurements that the obtained values are reasonably consistent when a comparison is made between specimens. More specifically, the measured data for the as-cast sample and the specimen irradiated with a fluence of 4.04 J/cm² always displayed tensile residual stress, while measured values between these two groups are rather different. In contrast, all measured data points on the sample treated with a fluence of 3.42 J/cm² showed compressive residual stress. These results are in-line with the micro-hardness measurements presented earlier. In particular, the observed hardening of the surface for an applied fluence of 3.42 J/cm² is accompanied with the introduction of compressive residual stress, while the softening effect observed for the fluence of 4.04 J/cm² is associated with the presence of tensile residual stress.
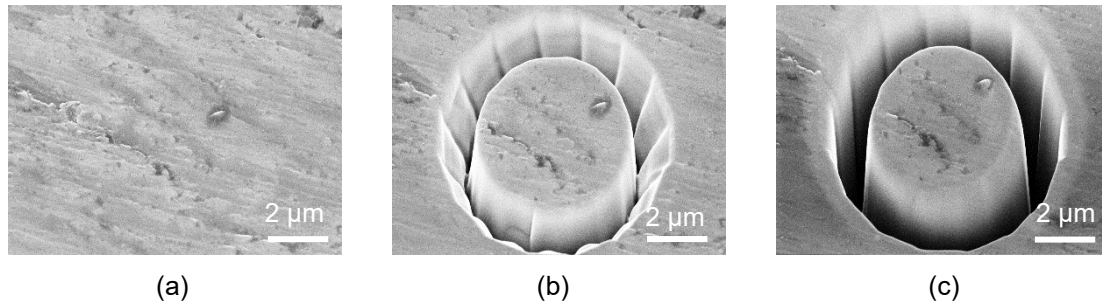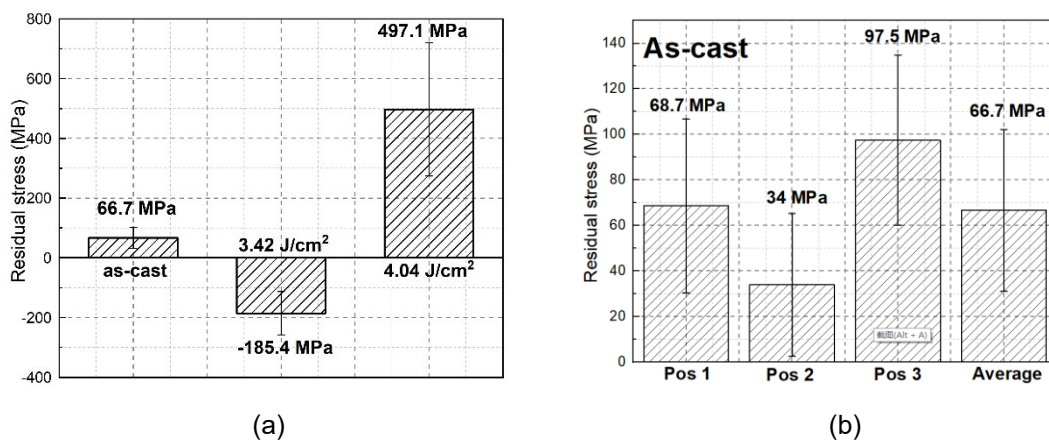

(a) (b) (c)

Fig. 3. Representative SEM images taken during FIB milling of a ring-core feature on the as-cast sample: (a) original surface; (b) after milling two layers (c) upon completion of the process, i.e. after milling 14 layers.

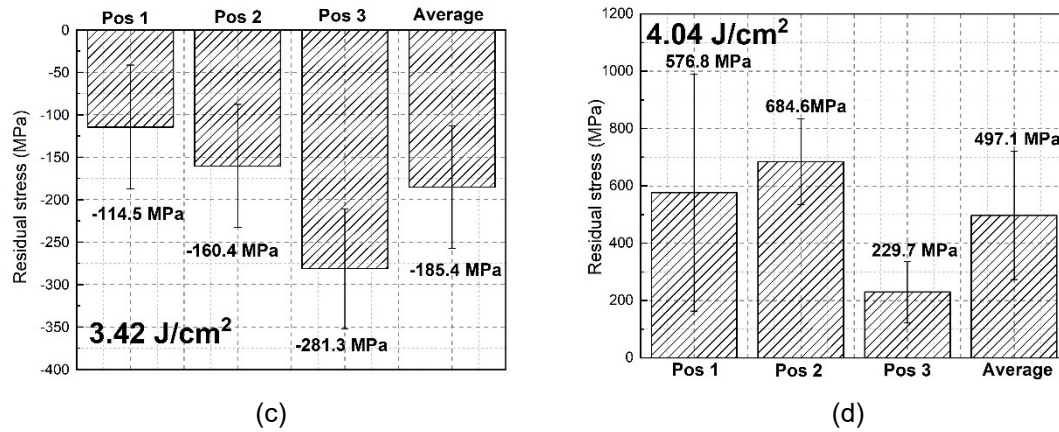(a) (b)

(c)   (d)

Fig. 4. (a) Comparison of average near-surface residual stress between the selected Vitreloy 105 samples; individual and average residual stress values for (b) the as-cast sample; (c) the hardened sample LSM treated with a fluence of 3.42 J/cm^2; (d) the softened sample LSM treated with a fluence of 4.04 J/cm^2.

3.4. Microstructure analysis

Fig. 5 shows the XRD patterns of the Vitreloy 105 BMG prior to and after LSM operations. As can be seen from this figure, the XRD pattern of the as-cast sample shows an overall amorphous halo with two crystalline peaks. These were assessed to correspond to the $CuZr_2$ phase. Thus, it can be said that the commercial vacuum injection moulding process used to cast the original alloy did not lead to the synthesis of fully amorphous specimens. After laser irradiation with the fluence of 3.42 J/cm^2, two crystalline peaks of Al_2NiZr_6 [35] and an additional $CuZr_2$ peak were introduced. In contrast, with a higher laser fluence of 4.04 J/cm^2, no new crystalline phases formed and the intensity of the original $CuZr_2$ peaks was even reduced. Moreover, as seen in Fig. 5(b), which shows an enlarged view of the XRD patterns, the location of the diffraction peak corresponding to the $CuZr_2$ phase at 25.18° shifted to a slightly lower angle. This smoothened profile and the small change in location of the crystalline peak may be correlated with the formation of an amorphous microstructure [36].
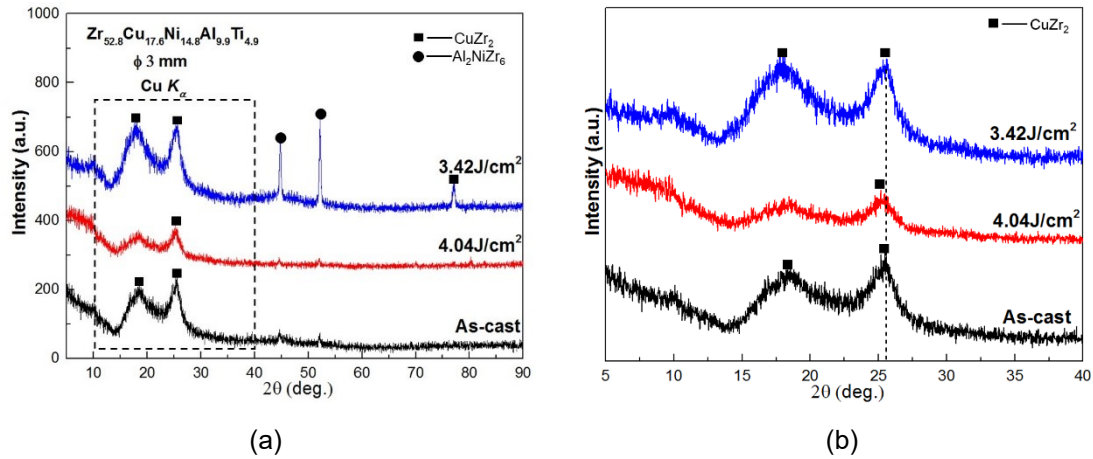
Fig. 5. (a) XRD patterns of Vitreloy 105 BMG specimens prior to and post laser surface melting; (b) enlarged view of (a) in the range 5-40°.

The fact that the sample treated with a fluence of 3.42 J/cm^2 displays a higher degree of crystallinity is in-line with related literature reported earlier since this specimen also exhibits an increased hardness. However, it is perhaps counter-intuitive to observe that when the fluence was further increased to 4.04 J/cm^2, then the surface became more amorphous. To confirm this particular observation, the surfaces of the as-cast and the LSMed samples were further compared using BSE micrographs, as shown in Fig. 6. It can be seen that a star shape crystalline phase was embedded in the amorphous matrix for the as-cast sample, in line with the XRD pattern reported earlier. In addition, this crystalline phase is also apparent on the surface of the sample irradiated with the fluence of 3.42 J/cm^2. In contrast, for the sample irradiated with the laser fluence of 4.04 J/cm^2, Fig. 6(c) indicates that a reduced occurrence of crystalline phase remained on the surface. The fact that a higher fluence led to the formation of a more amorphous layer near the surface may be attributed to the higher cooling rate induced by the increased laser fluence and consequent rapid heating and cooling cycles during LSM operations.
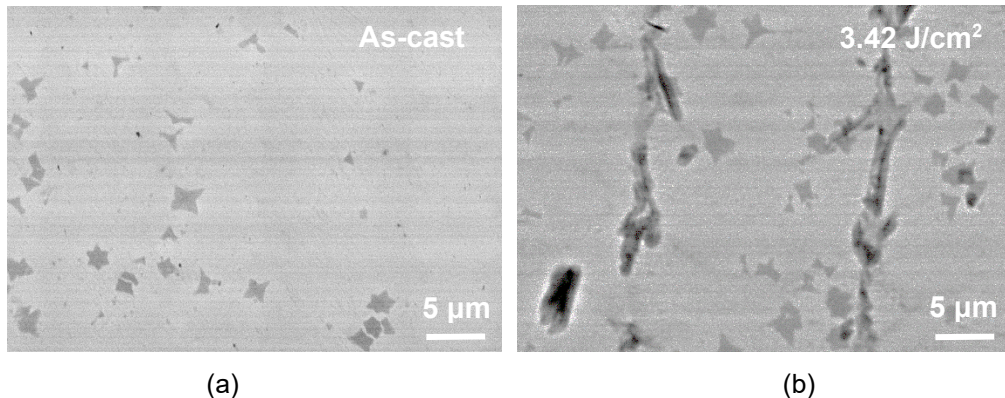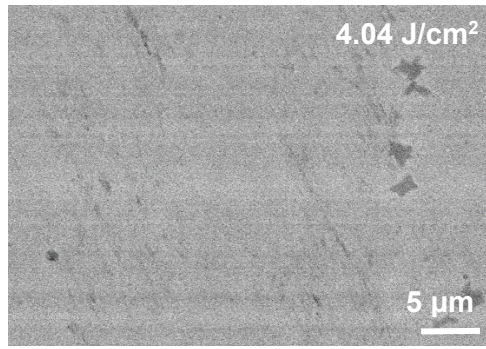
(c)

Fig. 6 BSE micrographs for three types of Vitreloy 105 surfaces: (a) as-cast (b) 3.42J/cm^2 (c) 4.04 J/cm^2

3.5. Nanoindentation tests

As reported in the literature, discontinuous depth bursts in load-depth (*P-h*) curves obtained via nanoindentation tests are considered to be directly related to shear banding activity, i.e. nucleation, propagation and blockage and/or cessation, inside and on the surface of BMGs [21, 23]. Thus, insight into the plastic deformation behaviour of BMGs can also be gained through the analysis of such discontinuous depth bursts, also referred to as serrated flows. Such data can be obtained via the continuous recording of the mechanical response of the specimen during a nanoindentation cycle. Fig. 7 shows the load-depth (*P-h*) curves of the as-cast and post-LSM samples. As could be expected, and in-line with the Vickers micro-hardness results, the maximum penetration depth was found to be the lowest (i.e. 924 nm) for the sample displaying a hardened surface post-LSM, while the highest penetration depth (i.e. 945 nm) was measured for the specimen with a softened surface. More interestingly, from the insets also included in this figure, which show magnified portions of the *P-h* curves, it is visible that serrated flows (discontinuous bursts) are quite prominent on both the as-cast sample and the specimen treated with 4.04 J/cm^2. In comparison, the *P-h* curve for the sample irradiated with 3.42 J/cm^2 is quite smooth.

In order to compare the serrated flow behaviour in a more systematic way, the depth-difference method was implemented on the recorded *P-h* data, as was also the case in previous studies [17, 21, 37]. In particular, when implementing this method, one single serrated flow event on the *P-h* curve is characterised by one sharp peak in the resulting depth-difference curve. The number and height of such peaks thus represent

the number and intensity of serrated flows on the corresponding P-h curves. The specific mathematical treatment of a P-h curve when applying this method can be found in reference [37]. In practice, the method relies on calculating the depth interval between two points along the x-axis (i.e. the horizontal axis of a P-h curve) corresponding to regular intervals of load along the y-axis (i.e. the vertical axis that records the indentation load). Results from applying the depth-difference method are also included in Fig. 7. From a purely qualitative observation of these graphs, it appears that the number and magnitude of the sharp peaks for the hardened sample post-LSM are reduced compared to data extracted for the as-cast sample. Again, solely from a qualitative perspective, the number and magnitude of such peaks seem to be slightly higher for the softened sample post-LSM. In order to provide a more quantitative analysis, Table 2 gives the number of peaks, which were recorded to be larger than 2 nm, as well as the total distance covered when adding all such peaks together, for all three samples. From this table, it becomes obvious that the sample softened following LSM with 4.04 J/cm^2 displayed the largest number of large-sized serrated flow events, while the hardened sample post-LSM, i.e. with a fluence of 3.42 J/cm^2, led to the smallest number. These results will be further discussed in the next section. It is quite apparent however, that the LSM operations conducted here could not only promote but also reduce serrated flow events for the treated Vitreloy 105 surface. In turn, this suggests an associated influence on the plastic deformation behaviour of this material post-LSM depending on the irradiation conditions.
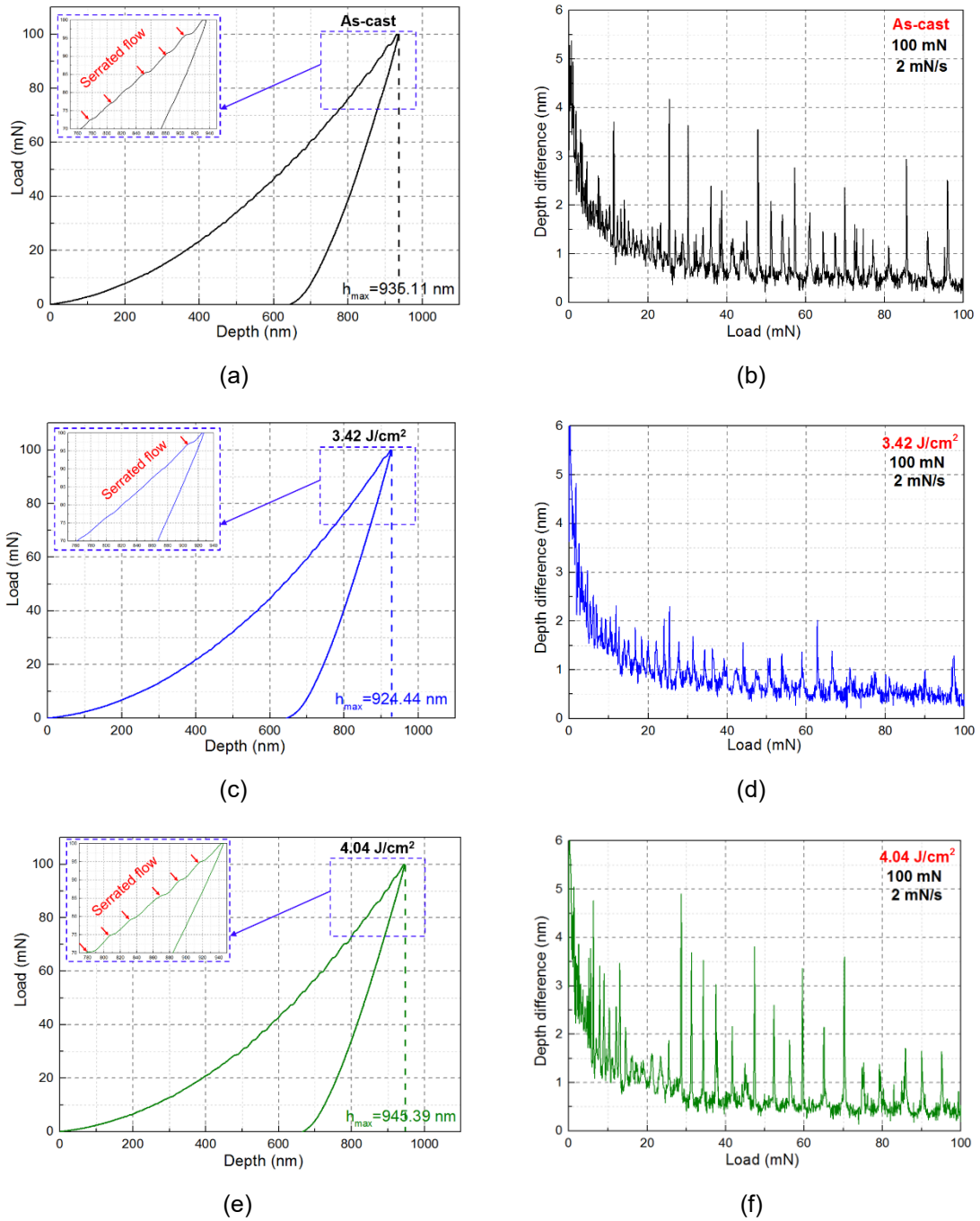
Fig. 7. Load-depth curves and corresponding depth-difference curves: (a) and (b) for the as-cast sample; (c) and (d) for the LSMed sample treated with 3.42J/cm²; (e) and (f) for the LSMed sample treated with 4.04J/cm².

Table. 2. Quantitative results obtained from the depth-difference method to characterise serrated flow events being over 2 nm in the load range 10-100 mN.

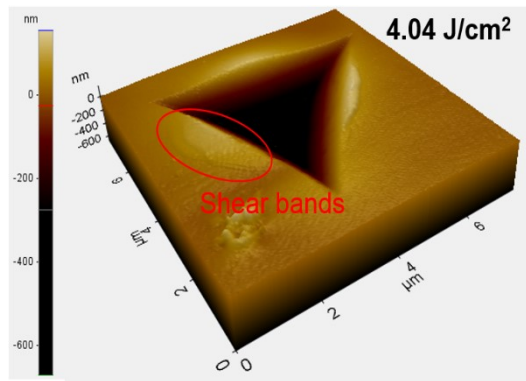|	As-cast	3.42 J/cm²	4.04 J/cm²
Number of depth-difference peaks being over 2 nm	20	5	26
Total distance when adding all depth-difference peaks being over 2 nm (nm)	53.45	10.76	72.95

In order to provide further experimental elements of discussion regarding the effect of LSM treatment on the shear banding behaviour near the surface of BMG specimens, the topography of typical pile-ups formed on the side of the nano-indents was analysed using AFM (see Fig. 8) and SEM data (see Fig. 9). Interestingly, numerous macroscopic shear bands were observed to reach the surface near nano-indents for the hardened sample post-LSM, while the softened sample displayed a reduced number of such surface shear bands and the as-cast sample almost none. The height of these pile-ups also tended to be highest for the hardened sample (see Fig. 8(d) as an example). The literature reports that an increased number of discrete bursts, or pop-ins, visible in the P-h curve corresponds not only to more pronounced shear banding activity but also this generally results in more shear bands reaching the surface near nano-indents [38, 39]. However, this is not the case in the present study. In fact, the number of shear band emerging on the surface is the highest for the sample displaying reduced shear banding activity. As will be discussed in the next section, this somewhat counter-intuitive observation indicates that residual stress might play an important role in the direction of propagation of shear bands, as was observed by Haag et al. [40].
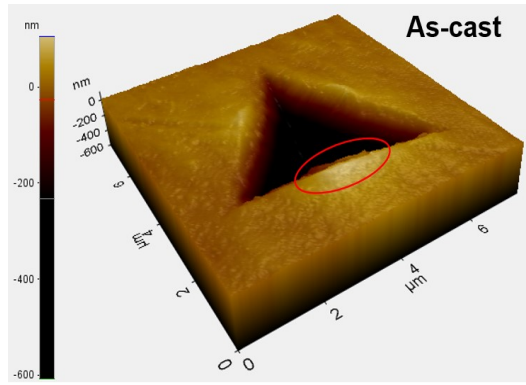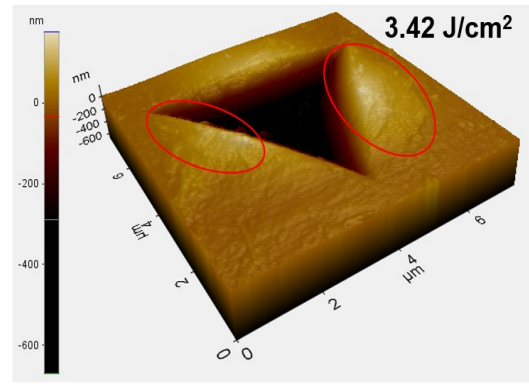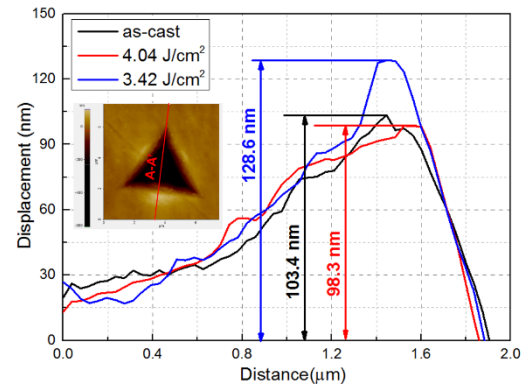
Fig. 8. Representative 3D topography of nano-indents on the: (a) as-cast sample; (b) LSMed sample treated with 3.42 J/cm²; (c) LSMed sample treated with 4.04 J/cm²; (d) corresponding line profiles from the data shown in (a), (b) and (c).
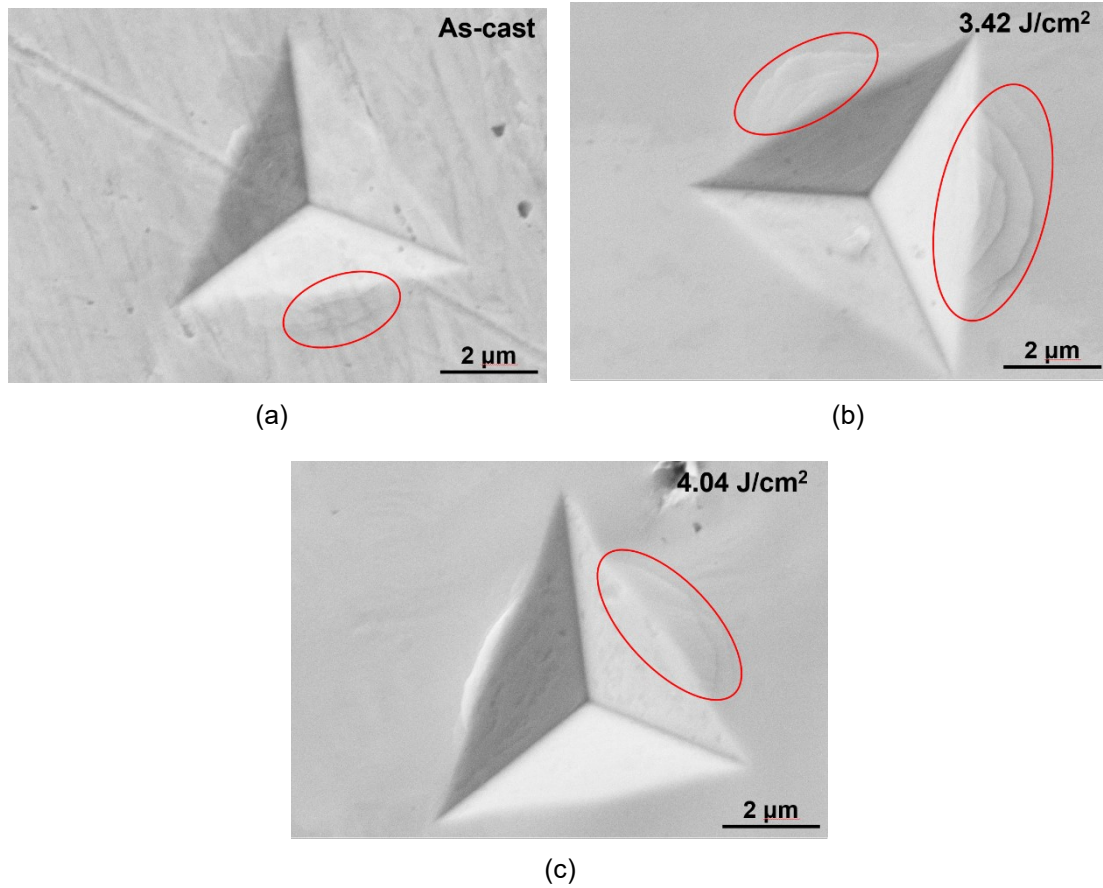
Fig. 9. Representative SEM micrographs of the residual indent morphology on the surface of (a) as-cast sample; (b) LSMed sample treated with 3.42 J/cm^2; (c) LSMed sample treated with 4.04 J/cm^2.

4. Discussion

4.1. Effect of LSM on the hardness of Vitreloy 105

An important outcome of this study is the experimental finding that, depending on the applied laser parameters, and especially the laser fluence, the surface of the irradiated Vitreloy 105 BMG could not only be softened but also hardened as a result of conducting LSM in ambient environment. It was also found that tensile residual stress was present on the softened surface, while compressive residual stress was measured on the hardened surface. Previous studies that focussed on the effect of residual stress on hardness generally tackled such investigations by measuring the hardness on the cross section of BMG beams pre-stressed elastically in bending [26, 41]. Findings from these reports suggest that a reduction in hardness takes place in regions of induced tensile stress, while such a correlation tends to be less obvious between increased pre-existing compressive stress and increased hardness, except at relatively high

stress level [40]. Thus, the increase in hardness following LSM treatment observed in this research may have been driven more substantially by the increase in the fraction of crystalline precipitates rather than by compressive residual stress. As reported earlier, the influence of the microstructure was also observed by Tariq et al. [19], Mudry et al. [20] and Huang et al. [21], albeit in the laser ablation regime for these former studies. Such a correlation was also found here as the hardened surface exhibited a more prominent $CuZr_2$ phase and the introduction of the Al_2NiZr_6 phase as well. With the increase in fluence, the prominence of crystalline precipitates was found to be reduced. As suggested earlier, this might be due to the increased cooling rate during the repeated cycles of irradiation at higher fluence. In addition, it is possible that the more pronounced laser thermal shock events, resulting from the increased fluence, could also have contributed to the reduced hardness via the introduction of shear bands within the material. Thus, in addition to the influence of the tensile residual stress, this could have led to further reduction of the hardness via shear band-induced softening [21].

4.2. Effect of LSM on the shear banding behaviour of Vitreloy 105

Following laser ablation of the Zr-based BMG Vitreloy 1, Huang et al. [21] found that laser-induced surface hardening was accompanied by a lack of shear bands reaching the surface during nanoindentation tests. In comparison, such shear bands could still be observed by these authors for as-cast and softened samples. Clearly, a different outcome is observed here as the sample for which LSM led to surface hardening displayed the more pronounced surface shear bands. Huang et al. [21] suggested that the lack of surface shear band in their case could have been due to the introduced secondary phase which impeded their propagation. In the current study, the higher proportion of crystalline precipitates for the sample in question did not prevent it from also being the specimen with the higher proportion of shear bands reaching the surface. The discrepancy between this outcome and that of Huang et al. [21] is explained by the role that the measured compressive residual stress should play in the present study. In particular, based on nanoindentation tests conducted on Cu-Zr-based BMG beams pre-stressed elastically, Haag et al. [40] reported that compressive residual stress could lead to a confined plastic deformation zone, increased material flow towards or at the sample surface and also higher pile-ups around indents. These authors also noted that, with tensile residual stress, no shear steps were found on the BMG surface following nanoindentation. The results presented here are also consistent with these findings from Haag et al. [40] when the effect of residual stress is considered. In

addition, similarly to these authors, higher pile-ups were also associated with the presence of compressive residual stress while a relatively smooth surface and lower pile-ups around the indents were observed for the sample exhibiting tensile residual stress (see Fig. 8).

However, one particular experimental result from the current study, which is different from the data presented by Haag et al. [40] is concerned with the observed serration behaviour between the as-cast sample and the specimen with compressive residual stress. Indeed, these authors found that both compressive and tensile residual stress led to an increase in the total serration length during nanoindentation when compared to the behaviour of the as-cast sample. This particular outcome was only verified here in the case of the specimen with tensile residual stress. Indeed, the sample displaying compressive residual stress showed a reduced overall distance of serrated flows (see Table 2). It is suggested that this discrepancy with Haag et al. [40] could be due to the difference in microstructure between the as-cast and LSMed samples in the current study. Indeed, it seems reasonable to suggest that the higher fraction of crystalline precipitates following LSM at the lowest fluence of 3.42 J/cm^2 impeded the propagation of shear bands and thus, led to a reduction of the measured total length of serrated flow events.

5. Conclusions

In this study, nanosecond laser surface melting in ambient atmosphere was exploited to modify the hardness, the microstructure and the shear banding behaviour of a Zr-based BMG, commercially known as Vitreloy 105. The Vickers micro-hardness and the residual stress on sample surfaces treated with different laser parameters were assessed. Moreover, the resulting microstructure on different irradiated surfaces was studied via X-ray diffraction and scanning electron microscopy. Finally, nanoindentation tests were conducted to evaluate the shear banding activity of the samples, while AFM and SEM were employed to characterise the residual indent morphology. Based on the obtained experimental results, the following conclusions can be made:

1. It was demonstrated that laser surface melting can not only soften the Vitreloy 105 material but also harden it, depending on the applied laser parameters. Among the parameters considered here, the laser fluence appeared to have the most prominent

effect on the micro-hardness compared to the scanning speed and the number of irradiation cycles.

2. For a fixed value of scanning speed and irradiation cycle, surface hardening was achieved with the lowest laser fluence considered. This outcome was accompanied with the introduction of compressive residual stress and an increased proportion of crystalline precipitates on the surface of the BMG. Based on the analysis of relevant literature, it may be possible that the increase in the crystalline fraction was the more important driving mechanism behind the observed hardening effect. In addition, with the introduction of compressive residual stress following LSM, overall reduced serrated flow but increased surface shear bands suggest that plastic deformation underneath the indenter became a highly localised activity.

3. The well-known surface softening effect was achieved for higher values of laser fluence when the combination of scanning speed and irradiation cycle led to a higher cooling rate. In this case, the presence of tensile residual stress and a reduction in the fraction of crystalline phases were observed. The introduction of tensile residual stress post-LSM operations promoted serrated flows and the likely distribution of shear banding activity well throughout the volume beneath the indenter.

Acknowledgements

Data availability

The raw and processed data required to reproduce these findings cannot be shared at this time as the data also forms part of an ongoing study. The corresponding author can be contacted in the future regarding access to the original data.

References

[1] M. Chen, A brief overview of bulk metallic glasses, NPG Asia Materials 3(9) (2011) 82-90.
[2] M. Ashby, A. Greer, Metallic glasses as structural materials, Scripta Materialia 54(3) (2006) 321-326.
[3] J.F. Löffler, Bulk metallic glasses, Intermetallics 11(6) (2003) 529-540.
[4] M.M. Trexler, N.N. Thadhani, Mechanical properties of bulk metallic glasses, Progress in Materials Science 55(8) (2010) 759-839.
[5] C. Schuh, T. Hufnagel, U. Ramamurty, Mechanical behavior of amorphous alloys, Acta Materialia 55(12) (2007) 4067-4109.
[6] Y. Zhang, W.H. Wang, A.L. Greer, Making metallic glasses plastic by control of residual stress, Nat Mater 5(11) (2006) 857-60.
[7] H.F. Li, Y.F. Zheng, Recent advances in bulk metallic glasses for biomedical applications, Acta Biomater 36 (2016) 1-20.
[8] M. Telford, The case for bulk metallic glass, Materials today 7(3) (2004) 36-43.
[9] S. González, J. Fornell, E. Pellicer, S. Suriñach, M.D. Baró, A.L. Greer, F.J. Belzunce, J. Sort, Influence of the shot-peening intensity on the structure and near-surface mechanical properties of $Ti_{40}Zr_{10}Cu_{38}Pd_{12}$ bulk metallic glass, Applied Physics Letters 103(21) (2013) 211907.
[10] Q. Wang, Y. Yang, H. Jiang, C.T. Liu, H.H. Ruan, J. Lu, Superior tensile ductility in bulk metallic glass with gradient amorphous structure, Sci Rep 4 (2014) 4757.
[11] J. Fu, Y. Zhu, C. Zheng, R. Liu, Z. Ji, Effect of laser shock peening on the compressive deformation and plastic behavior of Zr-based bulk metallic glass, Optics and Lasers in Engineering 86 (2016) 53-61.
[12] G. Wu, R. Li, Z. Liu, B. Chen, Y. Li, Y. Cai, T. Zhang, Induced multiple heterogeneities and related plastic improvement by laser surface treatment in CuZr-based bulk metallic glass, Intermetallics 24 (2012) 50-55.

[13] L. Zuo, R. Li, Y. Cheng, M. Meng, T. Zhang, A. Inoue, Influence of laser surface melting treatment on the surface composition and mechanical properties of a $Zr_{65}Al_{7.5}Ni_{10}Cu_{12.5}Ag_5$ bulk metallic glass, Journal of Non-Crystalline Solids 488 (2018) 63-68.

[14] B. Chen, Y. Li, M. Yi, R. Li, S. Pang, H. Wang, T. Zhang, Optimization of mechanical properties of bulk metallic glasses by residual stress adjustment using laser surface melting, Scripta Materialia 66(12) (2012) 1057-1060.

[15] Y. Cheng, S. Pang, C. Chen, T. Zhang, Size-dependent enhancement of plasticity by laser surface melting in $Zr_{55}Al_{10}Ni_5Cu_{30}$ bulk metallic glass, Journal of Alloys and Compounds 658 (2016) 49-54.

[16] B. Chen, S. Pang, P. Han, Y. Li, A.R. Yavari, G. Vaughan, T. Zhang, Improvement in mechanical properties of a Zr-based bulk metallic glass by laser surface treatment, Journal of Alloys and Compounds 504 (2010) S45-S47.

[17] H. Huang, M. Jiang, J. Yan, Softening of Zr-based metallic glass induced by nanosecond pulsed laser irradiation, Journal of Alloys and Compounds 754 (2018) 215-221.

[18] Y. Cheng, S. Pang, C. Chen, T. Zhang, Tensile plasticity in monolithic bulk metallic glass with sandwiched structure, Journal of Alloys and Compounds 688 (2016) 724-728.

[19] N.H. Tariq, B.A. Hasan, J.I. Akhter, Evolution of microstructure in $Zr_{55}Cu_{30}Al_{10}Ni_5$ bulk amorphous alloy by high power pulsed Nd:YAG laser, Journal of Alloys and Compounds 485(1-2) (2009) 212-214.

[20] S. Mudry, Y.S. Nykyruy, Y.O. Kulyk, Z. Stotsko, Influence of pulse laser irradiation on structure and mechanical properties of amorphous $Fe_{73.1}Nb_3Cu_{1.0}Si_{15.5}B_{7.4}$ alloy, Journal of Achievements in Materials and Manufacturing Engineering 61(1) (2013) 7-11.

[21] H. Huang, M. Jiang, J. Yan, The coupling effects of laser thermal shock and surface nitridation on mechanical properties of Zr-based metallic glass, Journal of Alloys and Compounds 770 (2019) 864-874.

[22] A.J. Lunt, A.M. Korsunsky, A review of micro-scale focused ion beam milling and digital image correlation analysis for residual stress evaluation and error estimation, Surface and Coatings Technology 283 (2015) 373-388.

[23] Y. Cao, X. Xie, J. Antonaglia, B. Winiarski, G. Wang, Y.C. Shin, P.J. Withers, K.A. Dahmen, P.K. Liaw, Laser Shock Peening on Zr-based Bulk Metallic Glass and Its Effect on Plasticity: Experiment and Modeling, Sci Rep 5 (2015) 10789.

[24] L. Wang, L. Wang, Z. Nie, Y. Ren, Y. Xue, R. Zhu, H. Zhang, H. Fu, Evolution of residual stress, free volume, and hardness in the laser shock peened Ti-based metallic glass, Materials & Design 111 (2016) 473-481.

[25] A.M. Korsunsky, T. Sui, E. Salvati, E.P. George, M. Sebastiani, Experimental and modelling characterisation of residual stresses in cylindrical samples of rapidly cooled bulk metallic glass, Materials & Design 104 (2016) 235-241.

[26] L. Wang, H. Bei, Y.F. Gao, Z.P. Lu, T.G. Nieh, Effect of residual stresses on the hardness of bulk metallic glasses, Acta Materialia 59(7) (2011) 2858-2864.

[27] X.H. Lin, W.L. Johnson, W.K. Rhim, Effect of Oxygen Impurity on Crystallization of an Undercooled Bulk Glass Forming Zr–Ti–Cu–Ni–Al Alloy, Materials Transactions 38 (1997) 473-477.

[28] Z. Bian, G. Chen, G. He, X. Hui, Microstructure and ductile–brittle transition of as-cast Zr-based bulk glass alloys under compressive testing, Materials Science and Engineering: A 316(1-2) (2001) 135-144.

[29] A.J. Lunt, N. Baimpas, E. Salvati, I.P. Dolbnya, T. Sui, S. Ying, H. Zhang, A.K. Kleppe, J. Dluhoš, A.M. Korsunsky, A state-of-the-art review of micron-scale spatially resolved residual stress analysis by FIB-DIC ring-core milling and other techniques, The Journal of Strain Analysis for Engineering Design 50(7) (2015) 426-444.

[30] C. Eberl, Digital Image Correlation and Tracking - File Exchange - MATLAB Central, 2019. https://uk.mathworks.com/matlabcentral/fileexchange/12413.

[31] E. Salvati, A.J. Lunt, T. Sui, A.M. Korsunsky, An investigation of residual stress gradient effects in FIB-DIC micro-ring-core analysis, Proceedings of the International MultiConference of Engineers and Computer Scientists, 2015.

[32] Z. Bian, M.X. Pan, Y. Zhang, W.H. Wang, Carbon-nanotube-reinforced $Zr_{52.5}Cu_{17.9}Ni_{14.6}Al_{10}Ti_5$ bulk metallic glass composites, Applied Physics Letters 81(25) (2002) 4739-4741.

[33] A. Greer, K. Rutherford, I. Hutchings, Wear resistance of amorphous alloys and related materials, International Materials Reviews 47(2) (2002) 87-112.

[34] I.C. Noyan, J.B. Cohen, Residual stress: measurement by diffraction and interpretation, Springer (2013).

[35] Z.-J. Yan, S.-E. Dang, X.-H. Wang, P.-X. Lian, Applicability of Johnson-Mehl-Avrami model to crystallization kinetics of Zr60Al15Ni25 bulk amorphous alloy, Transactions of Nonferrous Metals Society of China 18(1) (2008) 138-144.

[36] D. Gu, Y.-C. Hagedorn, W. Meiners, G. Meng, R.J.S. Batista, K. Wissenbach, R. Poprawe, Densification behavior, microstructure evolution, and wear performance of selective laser melting processed commercially pure titanium, Acta Materialia 60(9) (2012) 3849-3860.

[37] H. Huang, H. Zhao, Z. Zhang, Z. Yang, Z. Ma, Influences of Sample Preparation on Nanoindentation Behavior of a Zr-Based Bulk Metallic Glass, Materials, 5(6) (2012) 1033-1039.

[38] Y.I. Golovin, V. Ivolgin, V. Khonik, K. Kitagawa, A. Tyurin, Serrated plastic flow during nanoindentation of a bulk metallic glass, Scripta Materialia 45(8) (2001) 947-952.

[39] B.-G. Yoo, J.-Y. Kim, J.-i. Jang, Influence of indenter geometry on the deformation behavior of $Zr_{60}Cu_{30}Al_{10}$ bulk metallic glass during nanoindentation, Materials transactions 48(7) (2007) 1765-1769.

[40] F. Haag, D. Beitelschmidt, J. Eckert, K. Durst, Influences of residual stresses on the serrated flow in bulk metallic glass under elastostatic four-point bending – A nanoindentation and atomic force microscopy study, Acta Materialia 70 (2014) 188-197.

[41] L.Y. Chen, Q. Ge, S. Qu, J.Z. Jiang, Stress-induced softening and hardening in a bulk metallic glass, Scripta Materialia 59(11) (2008) 1210-1213.